OPTICA

Integrated quantum communication network and vibration sensing in optical fibers

Shuaishuai Liu,[1,2] Yan Tian,[1,2] Yu Zhang,[1,2] Zhenguo Lu,[1,2] Xuyang Wang,[1,2,3] and Yongmin Li[1,2,3,*]

[1]State Key Laboratory of Quantum Optics and Quantum Optics Devices, Institute of Opto-Electronics, Shanxi University, Taiyuan 030006, China
[2]Collaborative Innovation Center of Extreme Optics, Shanxi University, Taiyuan 030006, China
[3]Hefei National Laboratory, Hefei 230088, China
*yongmin@sxu.edu.cn

Received 24 July 2024; revised 4 November 2024; accepted 20 November 2024; published 18 December 2024

Communication and sensing technologies play crucial roles in various aspects of modern society. The seamless combination of communication and sensing systems has attracted significant interest in recent years. Without adding core devices, vibration-sensing functions can be integrated to build a quantum network with high efficiency and versatility. In this study, we propose and demonstrate a network architecture that integrates a downstream quantum access network (DQAN) and vibration sensing in optical fibers. By encoding the key information of eight users simultaneously on the sidemode quantum states of a single laser source and successively separating them using a specially designed narrow-bandwidth filter network, we achieved a secure and efficient DQAN with an average key rate of 1.94×10^4 bits per second over an 80 km single-mode fiber. Meanwhile, vibration locations with spatial resolutions of 131, 25, and 4 m at vibration frequencies of 100 Hz, 1 kHz, and 10 kHz, respectively, were implemented using the existing DQAN system infrastructure. The results indicate that the backward probe beam has a negligible effect on the DQAN system. Our integrated architecture provides a viable and cost-effective solution for building a quantum communication sensor network and paves the way for the functionality expansion of quantum communication networks. © 2024 Optica Publishing Group under the terms of the Optica Open Access Publishing Agreement

https://doi.org/10.1364/OPTICA.537655

1. INTRODUCTION

Quantum communication employs quantum states as carriers of quantum or classical information and plays a significant role in various applications, such as quantum key distribution (QKD) [1–6], quantum teleportation [7], quantum digital signatures [8], quantum secret sharing [8,9], and quantum e-commerce [10]. Although they have achieved significant breakthroughs, traditional QKD methods are limited to point-to-point communication. Quantum networks can overcome this limitation and extend two-user communication to multiple-user scenarios. Simple and cost-effective quantum network architectures and versatile features are crucial for the widespread application of future quantum networks.

Thus far, the demonstrated quantum networks can be classified into fully connected [11,12] and node-based [9,13–29] network architectures based on the network topology. The former utilizes untrusted entangled sources and dense wavelength-division multiplexing (DWDM) to connect all users fully. Although this architecture is robust and versatile, the number of wavelength channels determined by the permutation A_n^2 limits the number of users n. The latter is subdivided into untrusted relay node networks [13–15], trusted relay node networks [16–19], and point-to-multipoint centralized networks [9,20–28] depending on the type of node. An untrusted relay node network employs remote single-photon interferometry or Bell-state measurements to correlate user information while allowing nodes to be untrusted. This is currently limited to the implementation of network protocols for quantum conference key agreements [13–15] or quantum secret sharing [13]. A trusted relay node network is a fully connected point-to-point QKD link that can be used to build a large-scale network if each node is fully trusted. The point-to-multipoint centralized network architecture allows communication between the central node and multiple nodes to batch send or receive secret key information. This architecture shares the laser source and coding system with the transmitter, detector, and data-acquisition system at the receiver. Therefore, it can simplify the configuration and management of quantum networks and reduce the construction and maintenance costs of the system. Furthermore, it allows the other nodes to send or receive information even if a user node fails or disconnects.

The quantum access networks (QANs) provide the last-mile service by connecting a multitude of end users. They can significantly expand the number of users and are indispensable in quantum networks. Upstream QAN (UQAN): the quantum transmitter is located at the quantum network unit (QNU), and the keys are transmitted from the QNU to the quantum line terminal (QLT). This implies that QNU is responsible for generating and sending quantum signals to QLT, which measures the signals.

Downstream QAN (DQAN): in contrast to the upstream configuration, the quantum transmitter is located at the QLT, and the keys are transmitted from the QLT to the QNU. The QLT acts as a transmitter that generates and transmits quantum signals, whereas the QNU receives the signals [22,25–28]. UQAN typically adopts a time-division multiplexing scheme that divides the entire communication time into several time slots and precisely assigns the corresponding time slots to different users according to predefined rules. The clock synchronization of all users is a prerequisite for ensuring smooth system operation and is a complex and challenging task [22,28]. Compared to UQAN, DQAN can share complex and expensive encoding devices and make full use of the modulator bandwidth [25,27].

Optical fibers are the dominant transmission medium in modern telecommunication networks owing to their high bandwidth, low loss, and anti-electromagnetic interference. In addition to transmitting information, significant breakthroughs have been made in forward fiber sensing technology [30–35], which enables the monitoring and measurement of seismic activity and tsunamis by analyzing changes in the phase and polarization states of the forward-transmitted light field [30,31]. Distributed optical fiber sensing (DOFS) technology relies on light backscattering in optical fibers [36–38] and typically has a detection range not exceeding 150 km [38]. However, this technology requires high incident optical power, which is often dependent on an erbium-doped fiber amplifier (EDFA) to boost the input optical power [38] and is not compatible with QKD systems. In contrast, forward fiber sensing technology can implement fiber vibration sensing with a low input optical power and has a much longer sensing distance.

Enabling quantum communication network systems to sense the ambient environments, specifically by building a joint quantum communication sensor network, has gained significant attention [33]. This versatile system can expand the functionality of quantum communication networks by providing them with environmental perception ability, as well as enhanced communication performance through the sensing function. To this end, sensing capabilities should be introduced into quantum communication network architectures in a low-cost and compatible manner. More precisely, a seamless combination is desired, which means that the sensing system can operate without modifying the architecture of existing quantum communication networks.

In this paper, we propose and experimentally demonstrate a secure and efficient DQAN and verify the feasibility of the integration of the DQAN and vibration sensing in optical fibers. By adopting a multi-sideband modulation technique with a single modulator and a specially designed narrow-bandwidth filter network consisting of fiber-Bragg-grating-based fiber cavities (FBG-FCs), the central node simultaneously encodes the key information of eight users and then separates and sends the key information to each user. The proposed approaches enable point-to-multipoint simultaneous quantum communication without compromising system performance and substantially reduce the cost of quantum network deployment. We analyze the realistic security of the scheme by considering the imperfect modulation and filtering. The spatial resolution of the vibration localization reached 131 and 25 m at vibration frequencies of 100 Hz and 1 kHz, respectively. The added value of vibration sensing allows for the early detection of critical events such as earthquakes, tsunamis, landslides, and optical network surveillance, which may damage the optical infrastructure, without resorting to dedicated and expensive instruments.

2. PROTOCOL DESCRIPTION

A. DQAN Architecture

For a DQAN, the quantum server should encode multiple key information to enable the expansion of the number of users without significantly increasing the number of core devices. In addition, this ensures that the access performance of each user in DQAN would not be sacrificed with an increasing number of users, ensuring a robust and efficient quantum network.

Figure 1(a) shows our DQAN scheme, which is a star network architecture with the center node being the quantum server and the other nodes being the users, meeting the above requirements. We employed a quadrature phase-shift keying (QPSK) discrete modulation continuous-variable (CV) QKD protocol. The quantum server uses multi-sideband modulation techniques to encode n key information on different sidemodes of a single-frequency laser source with sideband frequencies f_j, $j \in \{1, 2, \ldots, n\}$. The sidemode coherent states prepared can be written as

$$|\alpha\rangle = |\alpha_k\rangle_{f_1} \otimes |\alpha_k\rangle_{f_2} \otimes \cdots \otimes |\alpha_k\rangle_{f_n},$$

$$|\alpha_k\rangle_{f_j} = \left|\alpha_{f_j} \exp\left[i(2k+1)\pi/4\right]\right\rangle, \quad k \in \{0, 1, 2, 3\}. \tag{1}$$

Here, each sidemode coherent state at f_j was independently and randomly chosen with an identical probability of $p_k = 1/4$. The total modulation variance of the quantum server is $V_A = \sum_{j=1}^{n} 2\alpha_{f_j}^2$ [normalized to shot noise units (SNUs)]. A single in-phase quadrature (IQ) modulator was employed in our system to implement encoding with multi-sideband modulation.

To separate the encoded quantum states and distribute them to the users, active optical switches [20,29] or one-to-N passive beam splitters [21,25,27] are typically used to split the information into different time slots or multiple pieces. Both methods require each user to be equipped with a high-speed acquisition system [39], including high-bandwidth-balanced homodyne detectors, a high-sampling-rate analog-to-digital convertor (ADC), and high-speed postprocessing to match the transmitter requirements. This configuration incurs additional costs and technical challenges. An optical-switch-based DQAN needs to frequently control the optical switch, while users have to wait for their allocated time slots. This intermittent key distribution method inevitably increases the additional overhead in terms of clock [40,41] and data synchronization, which could become a bottleneck in large-scale deployment. For the DQAN constructed using a passive beam splitter, the remaining users are considered potential eavesdroppers for the key distribution between each user and the quantum server. This results in excess loss of the quantum channel and significantly degrades the performance of the DQAN, particularly for a multitude of users [25,27].

To efficiently separate the sidemode quantum states without affecting the system performance, a narrow-band filtering system consisting of FBG-FC and optical circulators was designed, as shown in Fig. 1(b). There are two criteria for designing a fiber cavity. First, the free spectral region (FSR) $v_{FSR} = c/(2dl)$ should be larger than the frequency range of the entire sidemodes, where c is the speed of light in a vacuum, d is the refractive index of the fiber core, and l is the cavity length. Second, the linewidth (full width at half maximum, FWHM) of the cavity $\Delta v = v_{FSR}/F$ (F is the fineness of the cavity) should be wider than the bandwidth of each sidemode (determined by the system baud rate and modulation format) and narrower than the frequency spacing of

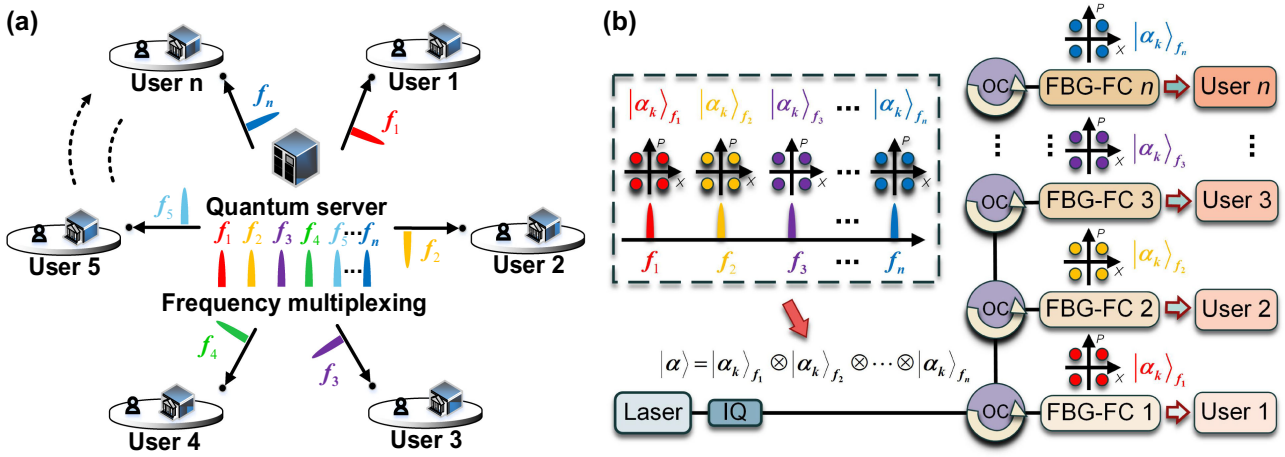

Fig. 1. Schematic of the downstream quantum access network (DQAN). (a) The DQAN architecture. The quantum server uses a coding system to prepare multiple sidemode quantum states at the sidebands of a single laser source, which are separated one by one using our self-designed filtering network and sent to the users over the quantum channels. The users measure and extract the key information located at pre-assigned sideband frequencies via the heterodyne detection. (b) Coding and filtering network. IQ, in-phase and quadrature modulator; OC, optical circulator; FBG-FC, fiber-Bragg-grating-based fiber cavity.

adjacent sidemodes. The above criteria ensure that each sidemode state can be faithfully separated with the least crosstalk with other sidemodes. Imperfect filtering may introduce excess noise and deteriorate system performance (see Supplement 1, Section 2 for details).

The separated sidemode states are sent to each user over an unsecured quantum channel. After measuring the received signals using heterodyne detection, the frequency and phase of each sidemode signal are recovered using the accompanying pilot tone. To extract the secret key from the raw data, the quantum server implements the standard secret key rate estimation procedure of QPSK CV-QKD, reverse data reconciliation, and private amplification.

B. Optical Fiber Vibration Sensing

Mechanical vibrations acting on the optical fiber can cause changes in the strain and refractive index of the fiber core, which further induces phase variations in the transmitted light. In our DQAN, users employ pilot tones to estimate the frequency offset and phase drift of the signal light transmitted from a quantum server. In this case, the acquired phase variation information can be applied to monitor the vibrations acting on the optical fibers in real time.

To achieve vibration localization, a two-way forward transmission is required (Fig. 2). To achieve this, users split a small portion of the laser and inject it into a quantum channel via an optical circulator. The quantum server measures the light transmitted from the users using heterodyne detection and estimates the phase variation information. The measured phase signals of the quantum server and users are given by [34]

$$\Delta\phi_{\mathrm{S}}(t) = 2\pi(f_{\mathrm{U}} - f_{\mathrm{S}})\,t + \left[\phi_{\mathrm{U}}^{\mathrm{laser}}(t-\tau) - \phi_{\mathrm{S}}^{\mathrm{laser}}(t)\right] + \phi_{\mathrm{vib}}(t-\tau_{\mathrm{S}}) + \phi_{\mathrm{S}}^{\mathrm{sys}}(t), \tag{2}$$

$$\Delta\phi_{\mathrm{U}}(t) = 2\pi(f_{\mathrm{S}} - f_{\mathrm{U}})\,t + \left[\phi_{\mathrm{S}}^{\mathrm{laser}}(t-\tau) - \phi_{\mathrm{U}}^{\mathrm{laser}}(t)\right] + \phi_{\mathrm{vib}}(t-\tau_{\mathrm{U}}) + \phi_{\mathrm{U}}^{\mathrm{sys}}(t), \tag{3}$$

where f_{S}, f_{U}, $\phi_{\mathrm{S}}^{\mathrm{laser}}$, and $\phi_{\mathrm{U}}^{\mathrm{laser}}$ denote the laser frequencies and phases of the quantum server and users, respectively. ϕ_{vib} is the phase fluctuation arising from the fiber link. $\tau_{\mathrm{S}} = L_{\mathrm{S}}/(c/d)$ and $\tau_{\mathrm{U}} = L_{\mathrm{U}}/(c/d)$ are the propagation delays from the vibration source to the quantum server and the user, respectively. $\tau = L/(c/d)$ is the propagation delay from the quantum server to the user, where $L = L_{\mathrm{S}} + L_{\mathrm{U}}$, L_{S}, and L_{U} are the distances from the vibration source to the quantum server and user, respectively. $\phi_{\mathrm{S}}^{\mathrm{sys}}$ and $\phi_{\mathrm{U}}^{\mathrm{sys}}$ are the equivalent (broadband) phase noises introduced by the receiver and fiber link, respectively.

To locate the vibration source at a certain frequency band, the first frequency offset terms in Eqs. (2) and (3) were compensated using frequency estimation. Next, digital bandpass filters were employed to suppress the laser phase and system noise and improve the signal-to-noise ratio (SNR). Subsequently, the delay difference $\Delta\tau = \tau_{\mathrm{S}} - \tau_{\mathrm{U}}$ was tracked by correlating the filtered phase signals $\Delta\phi_{\mathrm{S}}^{\mathrm{Filt}}(t)$ and $\Delta\phi_{\mathrm{U}}^{\mathrm{Filt}}(t)$ and finding the peak value of the correlation coefficients. At this stage, the vibration position is given by

$$L_{\mathrm{U}} = \frac{1}{2}\left(L - \frac{c\Delta\tau}{d}\right). \tag{4}$$

In the above, we have shown that our scheme can support both the DQAN and the vibrational sensing without modifying the existing hardware architecture and by only requiring an additional heterodyne detector.

C. Security Proof

The asymptotic secret key rate of each user in DQAN is given by (see Supplement 1, Section 1) [42–44]

$$K^{\infty} = R\left[\min_{\rho_{AB}\in\mathcal{S}} D(\mathcal{G}(\rho_{AB}) \,\|\, \mathcal{Z}[\mathcal{G}(\rho_{AB})]) - p_{\mathrm{pass}}\delta_{\mathrm{EC}}\right], \tag{5}$$

where R denotes the system repetition rate. $D(\rho\|\sigma) = \mathrm{Tr}(\rho\log_2\rho) - \mathrm{Tr}(\rho\log_2\sigma)$ denotes the quantum relative entropy,

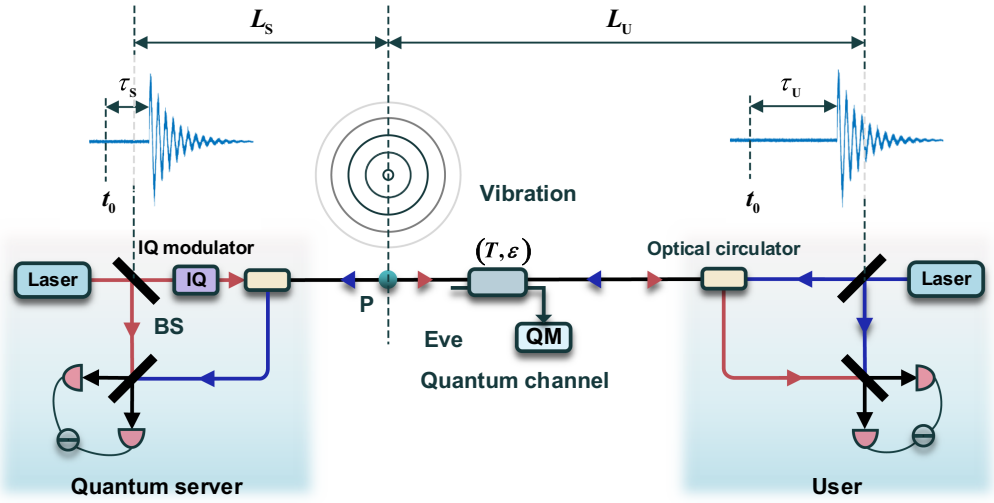

Fig. 2. Schematic of the optical fiber vibration sensing using the existing DQAN devices. The quantum server sends the quantum signals and pilot tones to the user. The user injects a weak probe beam back into the fiber through an optical circulator. Then, they measure and analyze the phase variations of the forward pilot tone and backward probe beam to achieve fiber vibrational localization through heterodyne detection and digital signal processing.

$\mathcal{G}$ denotes a fully positive and trace non-increasing map for classical post-processing processes, and ρ_{AB} denotes the joint state of the quantum server and the user after transmission through the quantum channel. Set S contains all density operators that are compatible with the experimental observations. $\mathcal{Z}$ describes a pinching quantum channel for obtaining the key mapping results, and p_{pass} denotes the sifting probability that the data from a given round will be used to generate the key. δ_{EC} denotes the leakage information of each signal pulse during error correction.

During the actual implementation of the DQAN, the imperfections of the devices can lead to potential security loopholes, which can be exploited by Eve [45,46]. In our scheme, the IQ modulator operates in a weak modulation regime, and only the positive first-order modulation sideband is employed. However, the residual mirror sideband from the finite sideband suppression ratio may leak some of the key information. Furthermore, the finite isolation degree of the filtering network that separates the different sidemodes can mix the signal fields of other users with those of the current user and cause information leakage.

To close these security loopholes, we established the security analysis model of the DQAN under the imperfect modulation and filtering attacks (see Appendices A and B for the detailed analysis). Based on the results of the security analysis, one of the constraints for minimizing the quantum relative entropy using convex optimization should be modified to

$$\text{Tr}_B[\rho_{AB}] = \sum_{l,h=0}^{3} \sqrt{p_l p_h}\, \langle \alpha'_h |\, \alpha'_l \rangle\, |l\rangle\langle h|_A,$$

$$\alpha'_{f_j} = g\alpha_{f_j}, \tag{6}$$

where $g = 1/(g_1\sqrt{1 - S_{j-1} - S_{j+1}})$ is the correction factor owing to imperfect modulation and filtering effects. α_{f_j} and α'_{f_j} are the measured complex amplitudes of the coherent states prepared for the jth user and corrected value, respectively. (see Appendix C for a detailed analysis).

3. EXPERIMENTAL INVESTIGATION

A. Experimental Setup

The experimental setup for the integrated DQAN and fiber vibration sensing is shown in Fig. 3(a). A DQAN consists of a quantum server and eight users connected via standard single-mode fiber spools. The quantum server performs multi-sideband modulation on a 100 Hz linewidth continuous-wave single-frequency laser (NKT-X15) using an IQ modulator (iXblue). The baud rate of the quantum symbols at each sideband is 50 MHz, and the center frequency of the quantum signals is $F_C = A + B\Delta\Omega_s$, $B \in (0, 1, \ldots, 7)$, where $A = 100$ MHz and $\Delta\Omega_s = 200$ MHz. In contrast to a quantum backbone network that supports large-capacity and high-speed key distributions, a QAN connects a multitude of end users, and low-speed communication is usually sufficient in most scenarios. The pilot tones that provide frequency and phase references for the quantum signals are frequency-multiplexed at the center frequency of the quantum signals. An arbitrary waveform generator (AWG) with a 10 Gsamples/s sampling rate converts the generated digital signals into analog signals to drive the IQ modulator. The multi-sideband quantum signals are separated through a self-designed filtering network and then sent to users through quantum channels.

Figure 3(b) depicts the measured power spectrum of the quantum signals and pilot tones. The resonance peak of the FBG-FC was precisely tuned to the center frequency of each sidemode using a piezoelectric transducer (PZT). The temperature of the FBG-FC was stabilized at room temperature with an accuracy of less than 0.01°C to prevent temperature drift, which would cause the frequency of the resonance peak of the FBG-FC to shift and the intensity of the quantum signals to fluctuate.

To investigate the fiber vibration sensing capability, we suspended 1.5 m of the single-mode fiber that belongs to the quantum channel over two fixed iron rods and simulated the vibration of outdoor suspension fiber cables by manually tapping on the rods or pulling the fiber, as shown in Fig. 4. For the high-frequency vibration simulations above 1 kHz, we installed a program-controlled PZT in the quantum channel [Fig. 3(a)], which generates sinusoidal modulation at 1 and 10 kHz.

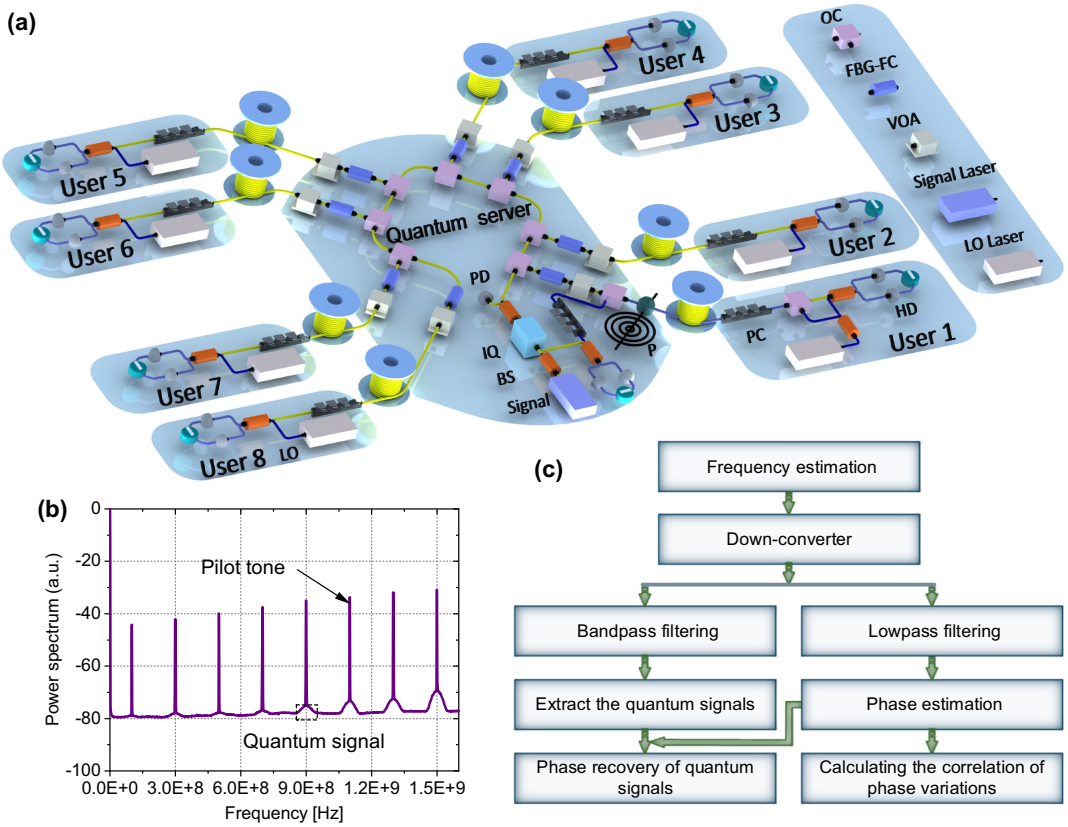

Fig. 3. (a) Experimental diagram of the integrated DQAN and fiber vibration sensing. BS, beam splitter; IQ, in-phase and quadrature modulator; PD, photoelectric detector; P, vibration position; PC, polarization controller; HD, heterodyne detector; OC, optical circulator; FBG-FC, fiber-Bragg-grating-based fiber cavity; VOA, variable optical attenuator. (b) Power spectrum of eight quantum signals and pilot tones. The frequency interval between adjacent quantum signals is 200 MHz. The increasing intensity of the quantum signals and pilot tones with the frequency is due to the compensation of filtering loss. (c) Digital signal procedures for extracting the quantum signals and vibration location.

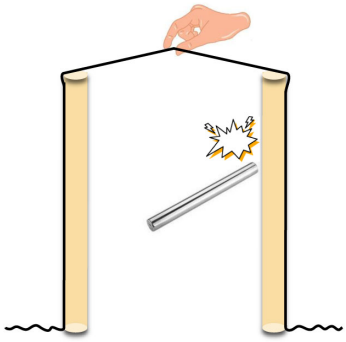

Fig. 4. Vibration simulation at 100 Hz. Two iron rods are securely fixed to simulate the outdoor utility poles. Subsequently, a 1.5 m fiber is suspended on the top end of the rods. By manually pulling the fiber or striking the iron rods, we simulate the vibrational response of a suspended optical cable to natural forces such as wind loads and seismic events in an outdoor environment.

After receiving the quantum signals, the users recovered the polarization states of the signal fields with a manual fiber polarization controller and performed the heterodyne detection with the local oscillator (LLO). The LLO was generated by an independent laser with a frequency difference of 50 MHz from the laser of the quantum server, and the local oscillator (LO) of all users was sourced from the same laser. A small portion of the laser with a power of −43 dBm for user 1 was inversely injected into the quantum channel via an optical circulator to provide a probe beam for fiber vibration sensing. The output signals from the heterodyne detectors at the quantum server and users were synchronously acquired using an oscilloscope at a sampling rate of 6.25 Gsamples/s.

The frequency and phase of the pilot tones and the quantum signals were extracted through a digital signal processing (DSP) module, as shown in Fig. 3(c). Using the retrieved relative frequencies of the pilot tone and probe beam, the quantum signals, pilot tones, and probe beams were down-converted to the baseband. A digital band-pass filter was employed to extract the quantum signals by filtering out pilot tones and high-frequency noise. The low-pass-filtered quadrature signals of the pilot tone and probe beam were utilized for phase estimation to recover the quantum signals and sense vibrations, respectively. For fiber vibration sensing, the quantum server and users correlated the retrieved phase variations of the forward pilot tones and backward probe beams.

B. Experimental Results

We successfully demonstrated the experimental validation of the combination of quantum communication and vibration-sensing techniques over fiber optic links of varying lengths, as shown in Fig. 3. The quantum server prepared and accurately separated the quantum states of all the eight users. To enhance the security of the measurement process, users employ LLO [47,48] for their

Table 1. Parameters of the Experimental System at 80 km[a]

Users	F_C (MHz)	V_{A_j} (SNU)	v_{el} (SNU)	η (%)	β (%)	ε (SNU)	T	K^{∞} (bps)
User 1	100	1.14	0.15	45	95	0.022	0.024	1.62×10^4
User 2	300	1.17	0.17	53	95	0.020	0.025	2.32×10^4
User 3	500	1.16	0.21	50	95	0.021	0.025	1.95×10^4
User 4	700	1.15	0.29	52	95	0.020	0.026	2.24×10^4
User 5	900	1.15	0.19	51	95	0.022	0.025	1.84×10^4
User 6	1100	1.20	0.17	54	95	0.021	0.025	2.02×10^4
User 7	1300	1.13	0.16	51	95	0.023	0.025	1.70×10^4
User 8	1500	1.16	0.16	54	95	0.022	0.024	1.83×10^4

[a]F_C, center frequency of the quantum signals; V_{A_j}, modulation variance of the quantum signals; v_{el}, electronic noise of the heterodyne detection; η, detection efficiency; β, reconciliation efficiency; ε, excess noise; T, transmittance of the quantum channel; K^{∞}, secret key rate.

measurements. Table 1 shows the experimental parameters of our integrated DQAN and vibration sensing for an 80 km standard single-mode fiber, including the modulation variance, excess noise, channel transmittance, detection efficiency, secret key rate, etc. Here, excess noise is used to indicate only the excess noise caused by the system itself, which is attributed to Eve's attack and is critical to the secret key rate (see Supplement 1, Section 2 for details).

The excess noise in our system mainly consists of the following components:

$$\varepsilon = \varepsilon_{\mathrm{CV-QKD}} + \varepsilon_{\mathrm{SASRS}} + \varepsilon_{\mathrm{Freq}} + \varepsilon_{\mathrm{Filt}}, \tag{7}$$

where $\varepsilon_{\mathrm{CV-QKD}}$ is the excess noise in a standard CV-QKD system [49], $\varepsilon_{\mathrm{SASRS}}$ is the Raman scattering noise due to the backward probe beam, $\varepsilon_{\mathrm{Freq}}$ is the frequency crosstalk noise, and $\varepsilon_{\mathrm{Filt}}$ is the filtering crosstalk noise. Notably, the Rayleigh scattering of the backward probe beam in fiber lies in the zero-frequency band, which differs from the frequency range of the quantum signals and is eliminated during the demodulation of the quantum signals. Here, we focus on the Raman scattering noise, frequency crosstalk noise, and filtering crosstalk noise (see Supplement 1, Section 2 for more details). In our experiment, the power of the backward probe beam was approximately −43 dBm, which induced a Raman scattering noise level of 4.07×10^{-6} SNU. To verify this prediction, we measured the excess noise of user 1 with and without the backward probe beam in the 10, 30, 50, and 80 km single-mode fibers (Fig. 5). The average values of excess noise without (with) the backward probe beam were almost the same: 0.0058 (0.0069), 0.0073 (0.0075), 0.013 (0.013), and 0.020 (0.019). These results indicate that the backward probe beam has a negligible effect on the DQAN system, which agrees with theoretical predictions.

Figure 6 shows the secret key rates of the DQAN system. The black pentagrams denote the key rate versus the length of the single-mode fibers. The red and blue lines denote the theoretical key rates using the experimental parameters and the PLOB bound [50], respectively. The experimental secret key rates are 2.39×10^6 (10 km), 6.32×10^5 (30 km), 2.03×10^5 (50 km), and 1.94×10^4 bits per second (bps) (80 km).

Figure 7 shows the recovered phases of the forward pilot tone and backward probe beam at different vibration frequencies. To achieve high-resolution positioning, selecting a digital bandpass filter of an appropriate type, bandwidth, and order is crucial to improve the SNR of the raw phases. An infinite impulse

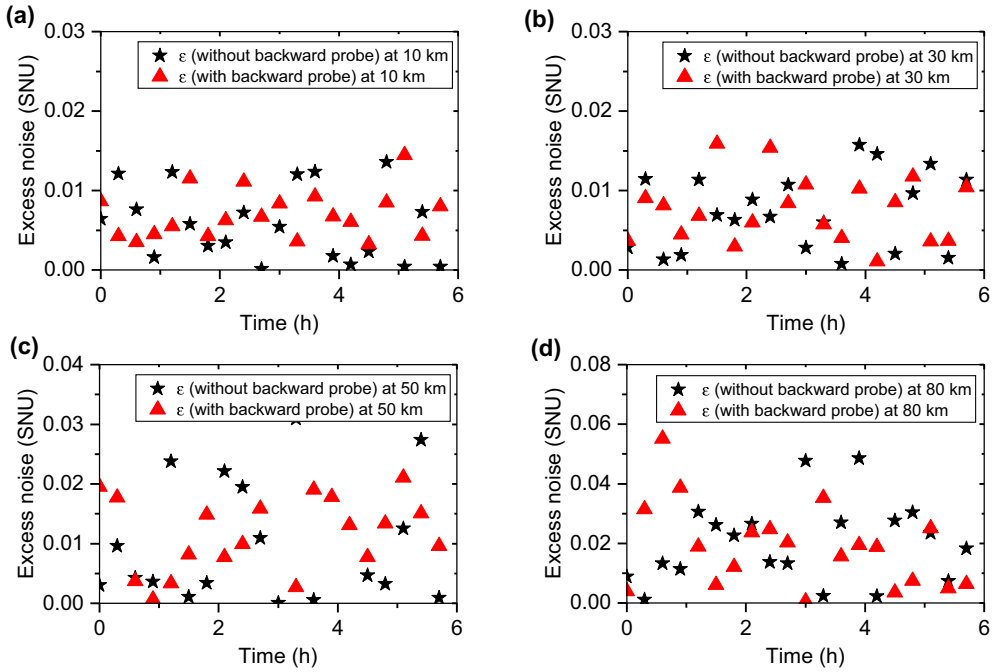

Fig. 5. Excess noise of user 1 with and without the backward probe beam. (a)–(d) Excess noise at 10, 30, 50, and 80 km of single-mode fibers. The black pentagram denotes the excess noise without the backward probe beam. The red triangle denotes the excess noise with the backward probe beam.

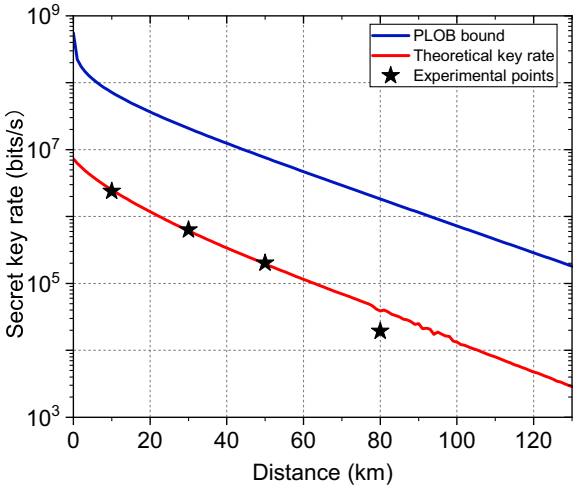

Fig. 6. Secret key rates of the DQAN. The blue solid line shows the PLOB bounds. The red solid line is the simulation key rate calculated using the experimental parameters. The black pentagrams are the experimental secret key rate (average value for the eight users) over 10, 30, 50, and 80 km single-mode fibers.

response (IIR) Butterworth filter was used for the vibration frequency at 100 Hz. In contrast, two cascaded finite impulse response (FIR) windowed filters were employed to filter the raw phases at 1 and 10 kHz (see Supplement 1, Section 3 for details). The relative delay of the vibration signals measured by the quantum server and users was obtained by calculating the correlation between the two extracted phase variations, and the vibration position was successively determined using Eq. (4). Figure 8 shows the spatial resolution of the vibration locations. The span between the blue and red solid lines indicates the maximum deviation between the experimentally measured and actual vibration positions. Based on the measured maximum deviation, the spatial resolutions were determined to be 131, 25, and 4 m at vibration frequencies of 100 Hz, 1 kHz, and 10 kHz, respectively.

Owing to the high sampling rate, our integrated quantum communication network and vibration sensing system achieved a spatial resolution higher than previous results that used the forward fiber sensing technology [30,33,34]. The vibration-sensing performances of the different systems are not directly comparable because of the different laser sources, sampling rates, levels of phase disturbance, and transmission distances in each system.

4. DISCUSSION AND CONCLUSION

In our proof-of-principle experiment, eight users shared the same local laser to provide their LO. Thus, each user requires a high-bandwidth heterodyne detector that can cover the frequency range of the respective sidemode, and the sampling rate of the ADC increases with the frequency of the sidemodes. In real-world network applications, where each user has its own local laser, its frequency can be tuned to be close to that of the received sidemodes. In this case, the quantum signals are shifted to the low-frequency range such that low-bandwidth heterodyne detectors and a low ADC sampling rate are sufficient to acquire the quantum signals. This feature significantly simplifies the measurement apparatus and reduces the cost of the DQAN. For practical applications of QAN, the cost of associated electronics (mainly electronic digital-to-analog converters, DACs) should be considered. In the scenario of a medium-scale group of 64 users, the DAC was deemed cost-effective. High-speed DACs are widely commercialized in modern coherent optical communication systems. Although the cost of a high-speed DAC is not low, it is shared by all users. For example, a modulation bandwidth of 20 GHz can support 100 users given that each user occupies a bandwidth of 100 MHz. In this case, the proposed integrated quantum communication and sensor network

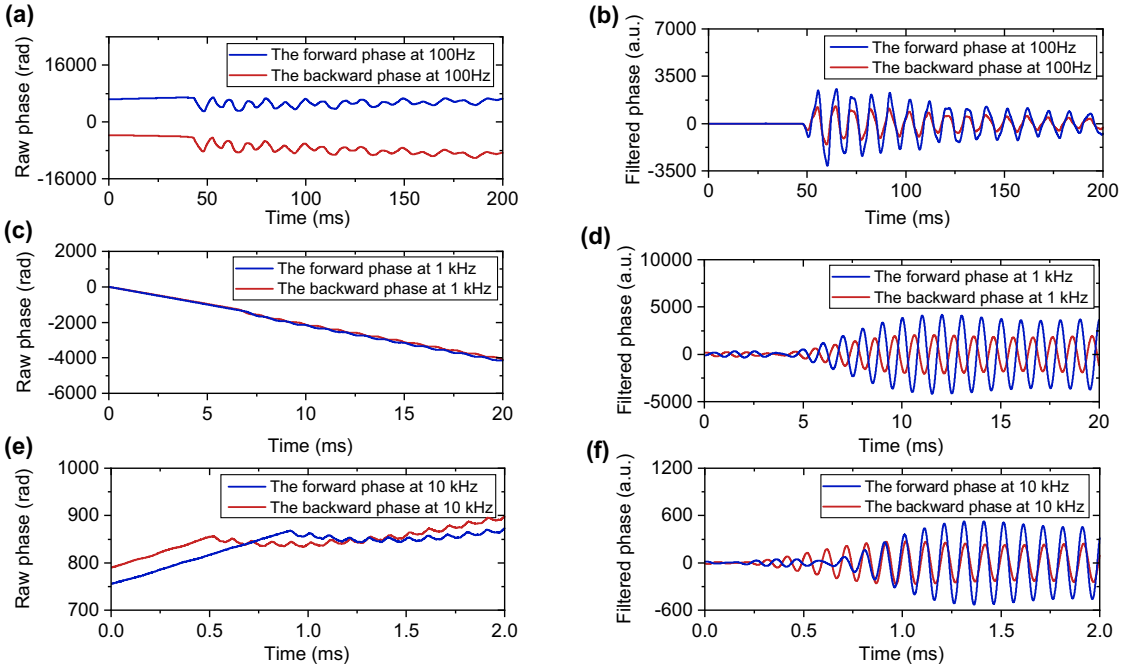

Fig. 7. Recovered phases at different vibration frequencies. The blue and red lines denote the raw phase variations of the forward pilot tone and backward probe beam at vibration frequencies of 100 Hz (a), 1 kHz (c), and 10 kHz (e), respectively. (b), (d), (f) Depict the filtered phase variations after digital bandpass filtering.

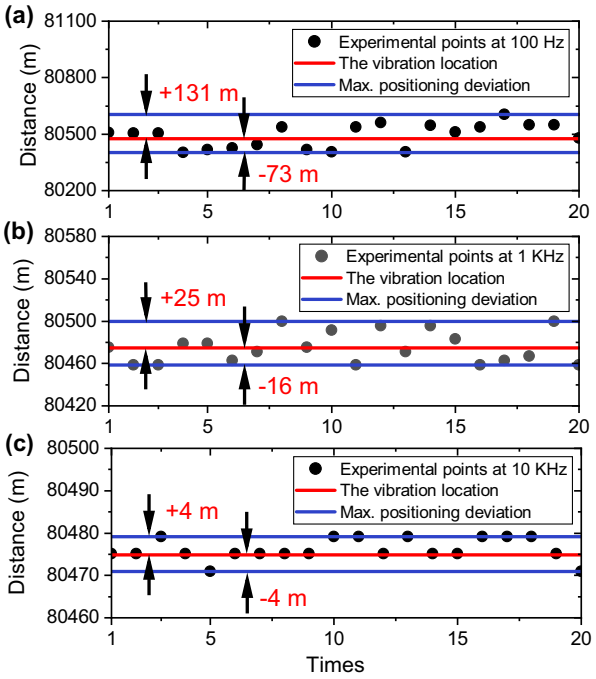

Fig. 8. Spatial resolution of the vibration location. The red solid lines denote the actual vibration position. The blue solid lines denote the maximum deviation of the vibration position. The black circles are the experimental points.

is cost-effective. Furthermore, the proposed network has an additional function for vibration sensing without incurring additional costs. With the rapid development of optoelectronic chips, their costs are expected to decrease significantly.

Notably, the DQAN is possible with the traditional 25 GHz DWDM technology [51]. However, this method is limited by the cost and footprint of a general DQAN. First, each user requires an independent laser with wavelength spaced of 25 GHz, which is commonly generated by distributed feedback laser arrays. One can also employ the optical frequency comb (OFC) with a line spacing of 25 GHz. Several methods can be used to generate an OFC, such as the external modulation of a narrowband continuous-wave laser and utilization of parametric frequency conversion in a Kerr-nonlinear microcavity. The OFCs in integrated photonic devices are not commercially available because of their limited power, complexity, and reliability [52]. Second, each user requires an independent modulator with driving circuits and a bias controller. Although low-speed DACs are simpler, multiple DACs and bias controllers are required to ensure that each modulator operates appropriately. Therefore, the overall cost of the lasers, modulators, and associated driving circuits and bias controllers is higher, and the entire volume is relatively large. The advantages of the 25-GHz-spaced DWDM-based DQAN lie in its high-speed communication capability, which is useful in special scenarios if its full bandwidth is employed. In this case, high-speed encoding and decoding are required.

For a transmission distance of 80 km, we chose an optical power of −43 dBm for the backward propagating channel. This is because when the optical power is reduced below −45 dBm, the measured phase accuracy drops sharply, making it difficult to accurately locate the vibration source. To ensure accuracy of the phase measurement, the optical power was increased by 2 dB. Although a higher input power does not significantly affect the system performance (the Raman noise is negligible), we found that increasing the optical power does not evidently improve the performance of vibration sensing. Therefore, we selected an optical power level of −43 dBm to balance the system performance and measurement accuracy. The ultimate limitations of our system lie in the level of excess noise of the longest distance CV-QKD experiment at present, which is 0.0081 SNU at 202.81 km of ultra-low-loss fiber, or 162.25 km in standard single-mode fiber [53]. We simulated the excess noise induced by Raman scattering as a function of the transmission distance (see Supplement 1, Section 2 for details). When the transmission distance reached 162.5 km, the excess noise increased to 0.0081 SNU, which determined the ultimate distance limitation for our system.

In our current experiment, a single-point vibration detection and location are demonstrated for one user. If the vibration frequencies are fully distinguishable, regardless of the vibration locations and occurrence times, multiple non-identical vibration sources can be located in principle using the frequency discrimination technique. However, the vibration frequencies of different vibration sources may overlap. In this case, the vibration waves arising from different vibration sources in the fiber link may cause constructive or destructive interference that can disturb the vibration location. To determine the correct location in such a case, the overlapping of the vibration waves should be avoided. This requires the minimal interval between the adjacent vibration events, which is determined by the time of the light propagation through the whole fiber link; in our case, it is $L/(c/d) \approx 4 \times 10^{-4}$ s. It is possible to achieve better location performance for both single-point and multi-point vibrations using advanced data processing methods such as Kalman filtering and machine learning. However, single-user vibration sensing can pinpoint vibrations that occur exactly on or very close to the fiber. If multiple users collaborate, the vibration signals far from the fiber can be located. For example, an earthquake epicenter can be located using two bidirectional fiber links [30]. More precisely, the coordinates of the epicenter are determined from the location point of the first arrival of the seismic wave along the fiber and simple geometry. Furthermore, remote timing synchrony between the forward and backward receivers is essential in practical applications and can be achieved by locking to GPS.

In conclusion, we proposed and demonstrated a scheme that integrates DQAN and fiber vibration sensing. This scheme requires only one transmitter to encode key information and can achieve simultaneous communication between a quantum server and multiple users. Using the existing infrastructure of the DQAN system and introducing only one heterodyne detector in the quantum server, fiber vibration detection and localization can be achieved without adverse effects on the DQAN. We also analyzed information leakage caused by imperfect modulation and quantum signal filtering and proposed corresponding countermeasures. Our results provide a new network architecture for future quantum network deployment and open a new avenue for multifunctional quantum networks.

APPENDIX A: SECURITY PROOF UNDER THE NEGATIVE SIDEBAND

For ideal carrier suppression single sideband (CS-SSB) modulation, the negative sideband is absent. In practice, the negative sidebands cannot be completely suppressed owing to imprecise locking of the bias points and modulation imbalance of the IQ modulator, and so on. Eve can extract key information by acquiring negative sidebands and raise security threats.

The modulation depths of the IQ modulator can be written as $\mu_j^{\mathrm{I}} = \mu_1 = \mu + \sigma$ and $\mu_j^{\mathrm{Q}} = \mu_{\mathrm{Q}} = \mu - \sigma$, where $\mu = V \cdot \pi/(2V_\pi)$, and V and V_π represent the drive voltage and the half-wave voltage of the IQ modulator, respectively. σ is a small value that characterizes the modulation imbalance between the I and Q signals. By inserting the expressions for the modulation depths into the output field of the IQ modulator, we obtain

$$E_{\mathrm{out}}(t) = \frac{1}{2}E_{\mathrm{in}}(t)\left(\sin\left[\sum_{j=1}^{n}\mu_j^{\mathrm{I}}\cos(\omega_j t)\right] + \sin\left[\sum_{j=1}^{n}\mu_j^{\mathrm{Q}}\sin(\omega_j t)\right]\exp\left(i\pi\frac{V_{\mathrm{PM}}}{2V_{\pi/2}}\right)\right), \tag{A1}$$

where $E_{\mathrm{in}}(t) = E_0\exp(i\omega_s t)$ is the input optical field of the IQ modulator. $V_{\mathrm{PM}} = V_{\pi/2}$ is the bias voltage between paths I and Q. After performing certain algebraic operations [54,55], Eq. (A1) can be rewritten as follows:

$$\begin{aligned} E_{\mathrm{out}}(t) &\approx E_{\mathrm{in}}(t)\,(U_1 + U_2) \\ &\approx \frac{E_0}{2}\sum_{j=1}^{n}\left(\mu\exp\left[i\left(\omega_s+\omega_j\right)t\right] + \sigma\exp\left[i\left(\omega_s-\omega_j\right)t\right]\right), \\ U_1 &= (-1)^{m+1}J_{2m-1}(\mu+\sigma)\sum_{j=1}^{n}J_0^{j-1}(\mu+\sigma)\cos\left[(2m-1)\omega_j t\right], \\ U_2 &= iJ_{2m-1}(\mu-\sigma)\sum_{j=1}^{n}J_0^{j-1}(\mu-\sigma)\sin\left[(2m-1)\omega_j t\right], \end{aligned} \tag{A2}$$

where $J_0^{j-1}(\mu+\sigma) \approx J_0^{j-1}(\mu-\sigma) \approx 1$, $J_1(\mu+\sigma) \approx (\mu+\sigma)/2$, and $J_1(\mu-\sigma) \approx (\mu-\sigma)/2$ are the Bessel functions of the first kind of orders 0 and 1, respectively.

Equation (A2) indicates that the IQ modulator produces negative sideband terms. In the experiment, we suppressed the negative sidebands by finely adjusting the phase and amplitude of the IQ modulation signals, and a suppression ratio greater than 30 dB was obtained. Considering that the negative first-order sideband $(E_0/2)\sigma\exp[i(\omega_s-\omega_j)t]$ is the dominant residual term under the weak modulation condition, the ratio of the positive first-order sideband to the total sidebands is approximated as

$$g_1 \approx \sqrt{\frac{\mu}{\mu+\sigma}} = \sqrt{\frac{1}{1.001}} \approx 0.9995. \tag{A3}$$

APPENDIX B: SECURITY PROOF UNDER IMPERFECT FILTERING

Figure 9(a) shows the measured transmission spectrum of the FBG-FC by an optical spectrum analyzer. The resonance peak in the black dashed box was selected to separate the different sidemodes. This was determined by the wavelength of the laser, the extinction ratio of the resonance peak, and the direction of the resonance wavelength movement when stretching the FBG-FC by PZT. For realistic filters with finite extinction ratios in secure stations of quantum servers, the filter network cannot fully reject the quantum signals of other users when selecting the quantum signal of the target user [Fig. 9(b)]. The leaked information may open security loopholes; for example, Eve can cooperate with dishonest users to perform an attack.

The normalized transmission spectrum of the FBG-FC can be expressed as a Lorentzian function:

$$T_v(f) = \frac{1}{\pi}\frac{\frac{1}{2}\Delta v}{(f-f_0)^2 + \left(\frac{1}{2}\Delta v\right)^2}, \tag{B1}$$

where f_0 is the center frequency of the resonance peak and Δv is the linewidth. In our experiment, the linewidth Δv of the FBG-FC was approximately 100 MHz. We considered only leaked information from adjacent users (leaked information from non-adjacent users is negligible). Using Eq. (B1), the intensities of the jth sidemodes' key information obtained by the $(j-1)$th user, jth user,

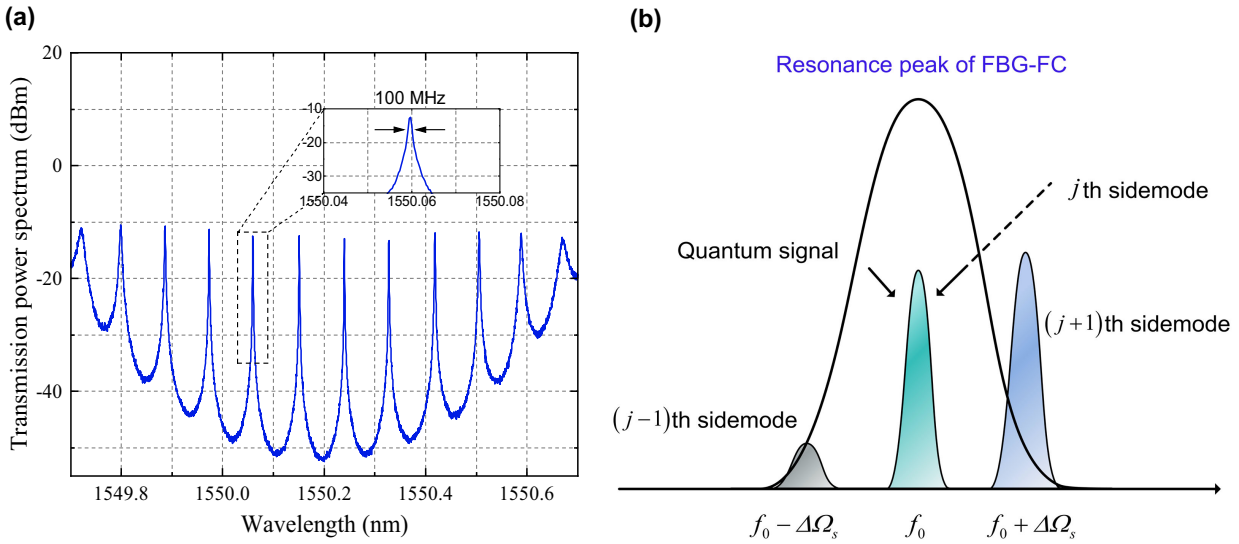

Fig. 9. Schematic of imperfect filtering. (a) Transmission power spectrum of FBG-FC. The resonance peak in the dashed box is employed to separate the different sidemodes. Three factors are considered to select the resonance peak: the wavelength of the laser, the extinction ratio of the transmitted peak, and the direction of the resonance wavelength movement when stretching the FBG-FC by PZT. The linewidth of the FBG-FC is approximately 100 MHz, and the frequency interval between the adjacent users is 200 MHz. The finite extinction ratio of the FBG-FC may result in the leakage of the adjacent users' key information. (b) Leakage due to imperfect filtering. The $(j-1)$th sidemode is the residual sidemode after the sidemode extraction by the $(j-1)$th user.

and $(j+1)$th user are given by

$$I_{j-1}=\int_{f_0+\Delta\Omega_s-\Delta f_q/2}^{f_0+\Delta\Omega_s+\Delta f_q/2} T_v(f)\,\mathrm{d}f,$$

$$I_j=\int_{f_0-\Delta f_q/2}^{f_0+\Delta f_q/2} T_v(f)\,\mathrm{d}f,$$

$$I_{j+1}=\int_{f_0-\Delta\Omega_s-\Delta f_q/2}^{f_0-\Delta\Omega_s+\Delta f_q/2} T_v(f)\,\mathrm{d}f. \tag{B2}$$

From Eq. (B2), the normalized intensity of the jth sidemode for the $(j-1)$th and $(j+1)$th users is given by

$$S_{j-1}=\frac{I_{j-1}}{I_{j-1}+I_j+I_{j+1}}=0.0683,$$

$$S_{j+1}=R_j\frac{I_{j+1}}{I_{j-1}+I_j+I_{j+1}}=0.0155, \tag{B3}$$

where $R_j=0.227$ denotes the residual reflectivity of the FBG-FC at the jth sidemode. Δf_q is the quantum signal bandwidth.

APPENDIX C: THE COUNTERMEASURES AGAINST THE NEGATIVE SIDEBAND AND NONIDEAL FILTERING ATTACKS

In the above discussion, we showed that nonideal CS-SSB modulation can result in the emergence of negative sidebands. However, imperfect filtering can cause the leakage of sidemodes to adjacent user channels. To close the security loopholes arising from these two aspects, we can correct the amplitudes of the prepared coherent states at the quantum server's site and rewrite Eq. (1):

$$|\alpha'\rangle=|\alpha'_k\rangle_{f_1}\otimes|\alpha'_k\rangle_{f_2}\otimes\cdots\otimes|\alpha'_k\rangle_{f_n},$$

$$|\alpha'_k\rangle_{f_j}=\left|\alpha'_{f_j}\exp\left[i(2k+1)\pi/4\right]\right\rangle,$$

$$\alpha'_{f_j}=\alpha_{f_j}/(g_1\sqrt{1-S_{j-1}-S_{j+1}}),\ k\in\{0,1,2,3\}, \tag{C1}$$

where α_{f_j} is the measured complex amplitude of the coherent states prepared for the jth user and α'_{f_j} is the corrected value. The correction here is equivalent to virtually incorporating leaked sidemode states into the prepared states [9,46]. More precisely, the correction specifically recovered the real modulation variance of the system. In this case, the system's channel parameters, including the channel transmittance and excess, can be correctly estimated, and a reliable secure key rate can be obtained. In this manner, the leaked information can be faithfully incorporated into the security frame and attributed to an insecure quantum channel.

Funding. National Natural Science Foundation of China (62175138, 62205188); Shanxi 1331KSC; Innovation Program for Quantum Science and Technology (2021ZD0300703).

Disclosures. The authors declare no conflicts of interest.

Data availability. The data underlying the results presented in this paper are not publicly available at this time but may be obtained from the authors upon reasonable request.

Supplemental document. See Supplement 1 for supporting content.

REFERENCES

1. F. Xu, X. Ma, Q. Zhang, *et al.*, "Secure quantum key distribution with realistic devices," Rev. Mod. Phys. **92**, 025002 (2020).
2. S. Pirandola, U. L. Andersen, L. Banchi, *et al.*, "Advances in quantum cryptography," Adv. Opt. Photon. **12**, 1012–1236 (2020).
3. C. Portmann and R. Renner, "Security in quantum cryptography," Rev. Mod. Phys. **94**, 025008 (2022).
4. Y. Zhang, Y. Bian, Z. Li, *et al.*, "Continuous-variable quantum key distribution system: past, present, and future," Appl. Phys. Rev. **11**, 011318 (2024).
5. J. Yin, Y.-H. Li, S.-K. Liao, *et al.*, "Entanglement-based secure quantum cryptography over 1,120 kilometres," Nature **582**, 501–505 (2020).
6. Y. Liu, W.-J. Zhang, C. Jiang, *et al.*, "Experimental twin-field quantum key distribution over 1000 km fiber distance," Phys. Rev. Lett. **130**, 210801 (2023).
7. S. Pirandola, J. Eisert, C. Weedbrook, *et al.*, "Advances in quantum teleportation," Nat. Photonics **9**, 641–652 (2015).
8. S. Richter, M. Thornton, I. Khan, *et al.*, "Agile and versatile quantum communication: signatures and secrets," Phys. Rev. X **11**, 011038 (2021).
9. S. Liu, Z. Lu, P. Wang, *et al.*, "Experimental demonstration of multiparty quantum secret sharing and conference key agreement," npj Quantum Inf. **9**, 92 (2023).
10. X.-Y. Cao, B.-H. Li, Y. Wang, *et al.*, "Experimental quantum e-commerce," Sci. Adv. **10**, eadk3258 (2024).
11. S. Wengerowsky, S. K. Joshi, F. Steinlechner, *et al.*, "An entanglement-based wavelength-multiplexed quantum communication network," Nature **564**, 225–228 (2018).
12. S. K. Joshi, D. Aktas, S. Wengerowsky, *et al.*, "A trusted node–free eight-user metropolitan quantum communication network," Sci. Adv. **6**, eaba0959 (2020).
13. Y. Fu, H.-L. Yin, T.-Y. Chen, *et al.*, "Long-distance measurement-device-independent multiparty quantum communication," Phys. Rev. Lett. **114**, 090501 (2015).
14. F. Grasselli, H. Kampermann, and D. Bruß, "Conference key agreement with single-photon interference," New J. Phys. **21**, 123002 (2019).
15. S. Zhao, P. Zeng, W.-F. Cao, *et al.*, "Phase-matching quantum cryptographic conferencing," Phys. Rev. Appl. **14**, 024010 (2020).
16. M. Peev, C. Pacher, R. Alléaume, *et al.*, "The SECOQC quantum key distribution network in Vienna," New J. Phys. **11**, 075001 (2009).
17. D. Stucki, M. Legré, F. Buntschu, *et al.*, "Long-term performance of the SwissQuantum quantum key distribution network in a field environment," New J. Phys. **13**, 123001 (2011).
18. M. Sasaki, M. Fujiwara, H. Ishizuka, *et al.*, "Field test of quantum key distribution in the Tokyo QKD network," Opt. Express **19**, 10387–10409 (2011).
19. Y.-A. Chen, Q. Zhang, T.-Y. Chen, *et al.*, "An integrated space-to-ground quantum communication network over 4,600 kilometres," Nature **589**, 214–219 (2021).
20. T.-Y. Chen, J. Wang, H. Liang, *et al.*, "Metropolitan all-pass and inter-city quantum communication network," Opt. Express **18**, 27217–27225 (2010).
21. I. Choi, R. J. Young, and P. D. Townsend, "Quantum information to the home," New J. Phys. **13**, 063039 (2011).
22. B. Fröhlich, J. F. Dynes, M. Lucamarini, *et al.*, "A quantum access network," Nature **501**, 69–72 (2013).
23. C. H. Park, M. K. Woo, B. K. Park, *et al.*, "2 × N twin-field quantum key distribution network configuration based on polarization, wavelength, and time division multiplexing," npj Quantum Inf. **8**, 48 (2022).
24. H. H. Brunner, C.-H. F. Fung, M. Peev, *et al.*, "Demonstration of a switched CV-QKD network," EPJ Quantum Technol. **10**, 38 (2023).
25. Y. Huang, T. Shen, X. Wang, *et al.*, "Realizing a downstream-access network using continuous-variable quantum key distribution," Phys. Rev. Appl. **16**, 064051 (2021).
26. Y. Xu, T. Wang, H. Zhao, *et al.*, "Round-trip multi-band quantum access network," Photon. Res. **11**, 1449–1464 (2023).
27. D. Qi, X. Wang, Z. Li, *et al.*, "Experimental demonstration of a quantum downstream access network in continuous variable quantum key distribution with a local oscillator," Photon. Res. **12**, 1262–1273 (2024).
28. X. Wang, Z. Chen, Z. Li, *et al.*, "Experimental upstream transmission of continuous variable quantum key distribution access network," Opt. Lett. **48**, 3327–3330 (2023).

29. X.-Y. Chang, D.-L. Deng, X.-X. Yuan, *et al.*, "Experimental realization of an entanglement access network and secure multi-party computation," Sci. Rep. **6**, 29453 (2016).
30. G. Marra, C. Clivati, R. Luckett, *et al.*, "Ultrastable laser interferometry for earthquake detection with terrestrial and submarine cables," Science **361**, 486–490 (2018).
31. Z. Zhan, M. Cantono, V. Kamalov, *et al.*, "Optical polarization–based seismic and water wave sensing on transoceanic cables," Science **371**, 931–936 (2021).
32. M. Cantono, J. C. Castellanos, V. Kamalov, *et al.*, "Seismic sensing in submarine fiber cables," in *European Conference on Optical Communication (ECOC)* (2021), pp. 1–3.
33. J.-P. Chen, C. Zhang, Y. Liu, *et al.*, "Quantum key distribution over 658 km fiber with distributed vibration sensing," Phys. Rev. Lett. **128**, 180502 (2022).
34. E. Ip, Y.-K. Huang, G. Wellbrock, *et al.*, "Vibration detection and localization using modified digital coherent telecom transponders," J. Lightwave Technol. **40**, 1472–1482 (2022).
35. Y. Zeng, X. Wang, W. Li, *et al.*, "Integrated communication and polarization sensing in self-homodyne coherent systems," Opt. Lett. **47**, 4684–4687 (2022).
36. H. He, L. Jiang, Y. Pan, *et al.*, "Integrated sensing and communication in an optical fibre," Light Sci. Appl. **12**, 25 (2023).
37. P. Jousset, T. Reinsch, T. Ryberg, *et al.*, "Dynamic strain determination using fibre-optic cables allows imaging of seismological and structural features," Nat. Commun. **9**, 2509 (2018).
38. P. Lu, N. Lalam, M. Badar, *et al.*, "Distributed optical fiber sensing: review and perspective," Appl. Phys. Rev. **6**, 041302 (2019).
39. H. Wang, Y. Li, Y. Pi, *et al.*, "Sub-Gbps key rate four-state continuous-variable quantum key distribution within metropolitan area," Commun. Phys. **5**, 162 (2022).
40. C. Agnesi, M. Avesani, L. Calderaro, *et al.*, "Simple quantum key distribution with qubit-based synchronization and a self-compensating polarization encoder," Optica **7**, 284–290 (2020).
41. T. Wang, Z. Zuo, L. Li, *et al.*, "Continuous-variable quantum key distribution without synchronized clocks," Phys. Rev. Appl. **18**, 014064 (2022).
42. J. Lin, T. Upadhyaya, and N. Lütkenhaus, "Asymptotic security analysis of discrete-modulated continuous-variable quantum key distribution," Phys. Rev. X **9**, 041064 (2019).
43. J. Lin and N. Lütkenhaus, "Trusted detector noise analysis for discrete modulation schemes of continuous-variable quantum key distribution," Phys. Rev. Appl. **14**, 064030 (2020).
44. S. Ghorai, P. Grangier, E. Diamanti, *et al.*, "Asymptotic security of continuous-variable quantum key distribution with a discrete modulation," Phys. Rev. X **9**, 021059 (2019).
45. H. Qin, R. Kumar, and R. Alléaume, "Quantum hacking: saturation attack on practical continuous-variable quantum key distribution," Phys. Rev. A **94**, 012325 (2016).
46. C. Li, L. Qian, and H.-K. Lo, "Simple security proofs for continuous variable quantum key distribution with intensity fluctuating sources," npj Quantum Inf. **7**, 150 (2021).
47. B. Qi, P. Lougovski, R. Pooser, *et al.*, "Generating the local oscillator "locally" in continuous-variable quantum key distribution based on coherent detection," Phys. Rev. X **5**, 041009 (2015).
48. A. A. E. Hajomer, I. Derkach, N. Jain, *et al.*, "Long-distance continuous-variable quantum key distribution over 100-km fiber with local oscillator," Sci. Adv. **10**, eadi9474 (2024).
49. F. Laudenbach, C. Pacher, C.-H. F. Fung, *et al.*, "Continuous-variable quantum key distribution with Gaussian modulation—the theory of practical implementations," Adv. Quantum Technol. **1**, 1800011 (2018).
50. S. Pirandola, R. Laurenza, C. Ottaviani, *et al.*, "Fundamental limits of repeaterless quantum communications," Nat. Commun. **8**, 15043 (2017).
51. Y. Wang, Y. Mao, W. Huang, *et al.*, "Optical frequency comb-based multi-channel parallel continuous-variable quantum key distribution," Opt. Express **27**, 25314–25329 (2019).
52. L. Chang, S. Liu, and J. E. Bowers, "Integrated optical frequency comb technologies," Nat. Photonics **16**, 95–108 (2022).
53. Y. Zhang, Z. Chen, S. Pirandola, *et al.*, "Long-distance continuous-variable quantum key distribution over 202.81 km of fiber," Phys. Rev. Lett. **125**, 010502 (2020).
54. N. Jain, I. Derkach, H.-M. Chin, *et al.*, "Modulation leakage vulnerability in continuous-variable quantum key distribution," Quantum Sci. Technol. **6**, 045001 (2021).
55. H. Wang, Y. Pan, Y. Shao, *et al.*, "Performance analysis for OFDM-based multi-carrier continuous-variable quantum key distribution with an arbitrary modulation protocol," Opt. Express **31**, 5577–5592 (2023).

219.26.34.73 (ts 2024-12-19 19:40:25)